Nanoscale

PAPER

View Article Online
View Journal | View Issue

Cite this: *Nanoscale*, 2017, **9**, 18022

Phonon coupling and transport in individual polyethylene chains: a comparison study with the bulk crystal†

Xinjiang Wang,[a] Massoud Kaviany[b] and Baoling Huang *[a]

Using the first-principles-based anharmonic lattice dynamics, we calculate the thermal conductivities (κ) of both bulk and single-chain polyethylene (PE) and characterize the mode-wise phonon transport and scattering channels. A significantly higher room-temperature axial thermal conductivity in single-chain PE (1400 W m^{-1} K^{-1}) is observed compared to bulk PE crystals (237 W m^{-1} K^{-1}). The reduction of scattering phase space caused by the diminished inter-chain van der Waals interactions explains the much larger κ in single-chain PE. Different from many previous studies, the thermal conductivity of single-chain PE is predicted to converge at a chain length of ~1 mm at 300 K. The convergence is explained by the indirect thermal resistance from momentum-conserving scatterings of long-wavelength phonons. It is also found that longitudinal phonon modes dominate the thermal transport in PE chains, while transverse phonon branches with quadratic dispersions contribute little to κ due to their vanishing group velocities and limited lifetimes in the long wavelength limit. The predicted high κ of bulk crystalline and single-chain PE show great potential for use of polymers in thermal management, and the unveiled phonon transport mechanisms offer guides for their molecule-level design.

Received 23rd August 2017,
Accepted 23rd October 2017

DOI: 10.1039/c7nr06216h

rsc.li/nanoscale

Introduction

Polymers are often classified as thermally resistive materials due to their low thermal conductivities (0.1 to 0.5 W m^{-1} K^{-1} near room temperature) in their amorphous state.[1] However, in applications ranging from cell-phone covers to the encapsulation of solar cells,[2] effective heat dissipation is imperative in stabilizing device performance and increasing lifetime. So, there is interest in thermally conductive polymers, and polymers with thermal conductivity κ above 10 W m^{-1} K^{-1} are already competitive in many applications such as *in situ* heat sinks in LED devices.[3] Improved κ has been reported for polymers with better crystallization. Significant increases of the axial thermal conductivity of polyethylene (PE) with large draw ratios have been observed ($\kappa \approx 42$ W m^{-1} K^{-1} at room temperature with a draw ratio ~350 (ref. 4)). This is because of the more aligned polymer chains in ultradrawn polymers which serve as efficient phonon transport paths along the axis (caused by the strong carbon–carbon covalent bonds, approaching the C–C bonds in diamond and graphite[5]).

Low dimensionality can also improve the thermal conductivity. For example, single-layer graphene and h-BN have larger thermal conductivities than their bulk lattices.[5,6] This is due to the reduction of scattering channels, mainly caused by symmetry constraints[7] and the removal of inter-layer coupling governed by strongly anharmonic van der Waals (vdW) forces.[8] By analogy, thermal transport in low-dimensional polymers may also benefit from the diminished vdW forces; for example, thermal conductivity up to 104 W m^{-1} K^{-1} has been reported for PE nanofibers of diameter around 50 nm.[9] The interest in single chain extraction[10] and nanoscale thermal conductivity measurement[11] continues.

Given the encouraging findings on polymers with large κ, it is desirable to unveil the thermal transport mechanisms in thermally conductive polymer structures and explore their potential in thermal management. However, direct measurements of single-crystalline or single-chain polymers remain very challenging due to the great difficulty of sample synthesis. Therefore, theoretical modeling and numerical simulations

[a]*Department of Mechanical and Aerospace Engineering, The Hong Kong University of Science and Technology, Clear Water Bay, Kowloon, Hong Kong.*
E-mail: mebhuang@ust.hk
[b]*Department of Mechanical Engineering, University of Michigan, Ann Arbor, MI 48109, USA*

† Electronic supplementary information (ESI) available: Some calculation details, including (i) the basic definitions of harmonic and anharmonic force constants; (ii) the expressions of symmetry constraints on the harmonic force constants and the illustration of the influence of symmetry constraints on the dispersion relation; (iii) the lattice constants, full-range dispersion of PE for a deeper insight into the lattice dynamics results; (iv) the thermal expansion coefficients of bulk PE at different temperatures to support the ability of first-principles calculations to recover the anharmonic properties; and (v) the convergence test of both bulk crystalline and single-chain PE with both mesh size and different approximations for the Dirac delta function. See DOI: 10.1039/c7nr06216h

have been used to investigate the thermal transport in these polymer structures. The axial κ of the crystalline PE has been predicted using molecular dynamics simulations (MD) to range from 47 to 310 ± 190 W m^{-1} K^{-1} (ref. 12 and 13) at room temperature. As for the thermal transport in a single polymer chain, there is an intense debate dating back to the early 1940s on whether the thermal conductivity of 1-D lattices converges[14] or not.[15] Conventional 1-D models often neglect the cross-axial vibrations and therefore it is still an open question whether they can accurately describe the phonon transport in a PE chain. The κ of quasi-1-D single polymer chains involving transverse motions has been predicted by atomic simulations, *e.g.*, MD[12,16–21] and the Green's function method,[22] finding larger values compared to the bulk lattice. However, bifurcations exist in simulated results over the convergence of an infinite chain. The κ of an individual PE chain is found to increase with the increase of length within the maximum simulation size (1000 unit cells), while a convergent thermal conductivity is reported for poly(*p*-phenylene).[20] The equilibrium MD results for 1-D PE chains are not conclusive either: convergent κ was reported[19] for some cases, while divergence was found under different initial conditions.[21]

Previous excellent computational studies helped to predict κ and unveil transport mechanisms in the 1-D polymer chain. However, the Green's function method[22] normally assumes ballistic phonon transport, and leads to a diverging κ with the increase of simulation size. On the other hand, classical MD simulations adopt empirical or semi-empirical potentials, and quantitative or even qualitative accuracy of the results essentially relies on the quality of these potentials. Furthermore, classical MD simulations are strictly valid only near or above the Debye temperature of the simulation system, while the high axial group velocity of a polymer crystal often results in a high Debye temperature (>1000 K),[23] which raises concerns about MD simulations near room temperature. In addition, non-equilibrium MD simulations require simulation dimensions much larger than the largest phonon mean free path (MFP),[24] while equilibrium MD simulations require sufficiently long simulation times. Both are challenging under the small intrinsic scattering strength.[25] Owing to these limitations, in recent years, first-principles lattice dynamics calculations of thermal transport properties based on the Boltzmann Transport Equation (BTE) have received great attention. The first-principles calculations have the advantages of accuracy and no fitting parameters (by solving the electron Kohn–Sham equation[26]). The BTE also makes it easier to conduct mode-wise analysis of thermal transport and directly reveal the scattering mechanisms.[27] This technique has been successfully used to study the phonon mode transport in many bulk crystals[28,29] and two-dimensional materials including graphene[25] and silicene.[30] However, to the best of our knowledge, so far there have been few studies on the mode-wise phonon transport in single polymer chains or single crystalline polymers using first-principles calculations and BTE. The closest work should be the lattice dynamics investigations into carbon nanotubes (CNT), which are also a quasi-1-D material.[28,31] It was revealed in precedent studies that the lack of Umklapp scatterings among acoustic phonons due to the rotational selection rule might lead to a divergent thermal conductivity in single-walled CNT.[28] But it is still unclear whether this phenomenon is universal in all chain materials.

In this study, we investigate the phonon coupling and transport in bulk crystalline polyethylene (PE) and single PE chains with first-principles calculations and numerical solution of the BTE. A high thermal conductivity of single-crystalline PE, comparable with that of aluminum, is found, which reveals great potential for crystalline polymers in thermal management. An even much higher but convergent κ in single-chain PE (up to 1400 W m^{-1} K^{-1} at 300 K) with vanished vdW forces is reported. The influence of various selection rules such as the conservation of momentum, angular momentum and energy on the thermal transport in single-chain PE is discussed. It is revealed that the strong momentum-conserving phonon scatterings of long-wavelength acoustic phonons contribute indirectly to the thermal resistance, leading to a convergent κ. Interestingly, the two transverse modes in the 1-D PE chain with quadratic dispersions only contribute a little to κ at room temperature, in contrast with the dominant κ contribution from the quadratic flexural mode in many 2-D materials[25] including graphene. The corresponding mechanisms of the above phenomena are then discussed.

Methodology

The phonon conductivity tensor κ of a crystal can be derived from the kinetic theory and a linear expansion of the equilibrium distribution with the temperature gradient,

$$\kappa_{ij} = -\frac{1}{N_o \Omega}\sum_{\lambda} \hbar\omega_\lambda v_\lambda^i n_\lambda^o \left(n_\lambda^o + 1\right) F_\lambda^j, \tag{1}$$

where λ represents a phonon mode with a wavevector $\boldsymbol{q}$ and phonon polarization p, ω is the phonon frequency, i, j are the Cartesian indices, v is the phonon group velocity, n_λ^o is the equilibrium phonon Bose–Einstein occupancy and is determined by $n_\lambda^o = [\exp(\hbar\omega/(k_B T) - 1)]^{-1}$ (k_B is the Boltzmann constant), Ω is the unit-cell volume and N_o is the total number of $\mathbf{q}$-points (within the first Brillouin zone). $\mathbf{F}$ is the linear phonon perturbation vector to expand the real occupancy $n_\lambda = n_\lambda^o + n_\lambda^o\,(n_\lambda^o + 1)\,\mathbf{F}_\lambda \cdot \nabla T$ and can be obtained by solving the BTE

$$-v^i(\lambda) n_\lambda^0 \left(n_\lambda^0 + 1\right) \frac{\hbar\omega_\lambda}{k_B T^2} = \tilde{P}_{\lambda,\lambda'} F_\lambda^i, \tag{2}$$

where $\tilde{P}_{\lambda,\lambda'}$ is the combined scattering matrix and is written as

$$\begin{aligned}\tilde{P}_{\lambda\lambda'} = P_\lambda^b \delta_{\lambda\lambda'} + \frac{1}{2}\sum_{\lambda'',\lambda'''} \left(P_{\lambda,\lambda'''}^{-\lambda''} + P_{\lambda,\lambda''}^{-\lambda'''} + P_{\lambda''',\lambda''}^{-\lambda}\right)\delta_{\lambda\lambda'} \\ + \sum_{\lambda''} \left(P_{\lambda,\lambda'}^{-\lambda''} + P_{\lambda,\lambda''}^{-\lambda'} + P_{\lambda',\lambda''}^{-\lambda}\right).\end{aligned} \tag{3}$$

Here $P_{\lambda,\lambda'}^{\lambda''}$, $P_{\lambda,\lambda''}^{\lambda'}$ and $P_{\lambda',\lambda''}^{\lambda}$ are the three-phonon scattering probabilities and P_λ^b the boundary scattering probability. All

the three phonon scattering processes should satisfy the energy conservation, *i.e.*, $\omega_\lambda \pm \omega_{\lambda'} \pm \omega_{\lambda''} = 0$, while quasi-momentums are constrained by $\mathbf{q} + \mathbf{q}' + \mathbf{q}'' = \mathbf{0}$ ($\mathbf{G}$), where $\mathbf{0}$ indicates a momentum conserving (normal) process and $\mathbf{G}$ (a non-zero reciprocal lattice vector) a non-conserving (Umklapp) process. The above expression is slightly different from some literature reports[32,33] but consistent with Chaput's simplification,[34] where, in principle, this definition is equivalent considering the time reverse symmetry and makes the expression of eqn (2) easier for implementation.[34]

In eqn (3), only $P^{\lambda''}_{\lambda,\lambda'}$ is expressed without loss of generalization as

$$P^{\lambda''}_{\lambda,\lambda'} = 2\pi n^{o}_{\lambda} n^{o}_{\lambda'} (n^{o}_{\lambda''} + 1)|V_{\lambda,\lambda',\lambda''}|^2 \, \delta(\omega_\lambda + \omega_{\lambda'} - \omega_{\lambda''}), \quad (4)$$

where δ is the Dirac delta function and V is the anharmonic force constant projected onto the eigenvector space.[35]

In a finite system, phonons experience an additional scattering with the boundary. Assuming a diffuse surface with elastic scattering, we have[36]

$$P^{b}_{\lambda} = \frac{|v_\lambda|}{l} n^{o}_{\lambda}(n^{o}_{\lambda} + 1) \quad (5)$$

where l is the Casimir effective length of the sample.

With the scattering operators, eqn (2) is solved first neglecting $\mathbf{F}_{\lambda'}$, $\mathbf{F}_{\lambda''}$ [corresponding to the single-mode relaxation-time model (SMRT)[37]] and later iteratively to obtain the exact solution using the preconditioned conjugate-gradient method[38] owing to its less stringent and faster convergence.

By comparing eqn (1) with the general thermal expression from SMRT $\kappa^{ij}(\lambda) = C_v(\lambda) v^i_\lambda v^j_\lambda \tau_\lambda$, where $C_v = \hbar\omega \partial n^0_\lambda / \partial T$ is modal heat capacity, we define an effective phonon lifetime,

$$\tau_{\mathrm{eff},\lambda} = \frac{k_B T^2}{\hbar\omega_\lambda} \cdot \frac{\mathbf{F}_\lambda \cdot \mathbf{v}_\lambda}{|v_\lambda|^2}. \quad (6)$$

Different from the relaxation time from SMRT, this newly defined lifetime conveys information on multiple phonon excitations and yet casts a simplified picture in the conventional frame for a better understanding. To calculate the thermal conductivity using the above equations, harmonic and anharmonic interatomic force constants are the only required inputs, which can be obtained using first-principles calculations through the finite displacement method.[39] More details of the calculation of lattice κ through the BTE method can be found elsewhere.[32,38,39]

For bulk PE, both relaxation and static energy calculations used the van der Waals (vdW) functional optB88-vdW[40,41] in addition to the local-density approximation (LDA), as implemented in the Vienna ab initio simulation package (VASP).[42,43] The structure was fully relaxed with a cutoff energy of 550 eV and an 11 × 15 × 31 k-point meshing scheme in the Brillouin zone. Then the original cell was expanded to a supercell of size 2 × 3 × 5 for the harmonic force constant calculations and 2 × 2 × 3 for the anharmonic ones. The thermal conductivity was calculated on different mesh sizes until convergence was reached.

For PE chains, the first-principles calculations are similar to those for the bulk, except that a vacuum slab of thickness 17 Å, large enough to diminish the influence of vdW forces, was used to accommodate the chain in the lateral directions (a and b in Fig. 1). The cross-sectional area of a single PE chain is defined the same as the average area one chain occupies in the PE crystal (~16.9 Å^2). After careful tests, the supercell sizes for the calculation of harmonic and anharmonic properties were chosen as 1 × 1 × 9 and 1 × 1 × 5, respectively, to ensure satisfactory convergence. Although the calculation process on the 1-D PE chain should be simpler than the bulk because of the disregard of cross-axial interactions, the results were found to be much more sensitive to the inevitable errors during the calculations. So, special techniques, including the symmetry constraints and the hyperspace tetrahedron method, were used for both the bulk and single-chain PE calculations.

The symmetry constraints on both harmonic and anharmonic force constants consist of permutational, translational, and rotational invariances and point group symmetries[44] (see the ESI† for more details). These symmetry constraints on the system not only reduce calculations, but also allow verifying the physicality of the results. There are intrinsic errors in the first-principles calculations, such as incomplete basis wavefunctions and small but finite residual stresses in the relaxed structures.[45] These small errors significantly influence the behavior of long-wavelength phonons (*i.e.*, dispersions in the long wavelength limit, see Fig. S1 in the ESI†). Therefore, the calculated force constants need to be adjusted to be physically reasonable, but such adjustments should be kept minimal to keep major lattice properties. Here we adopted the Lagrange multiplier method[46] to symmetrize the force constants. By utilizing this method, which implies the least discrepancy of the newly obtained force constants from the original, the irreducible elements were solved and the force constants satisfying all the symmetry constraints were deduced.

Another challenging issue in solving the BTE [eqn (2)] is the Dirac delta function estimation in eqn (4). This is conventionally accomplished by assuming a Gaussian distribution of the Dirac delta function with an arbitrarily assigned smearing factor, which is either constant[38] or adaptive.[32] However,

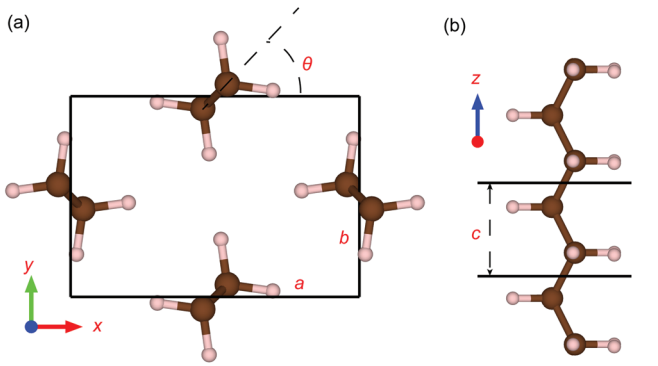

Fig. 1 (a) The structure of a bulk PE crystal in the cross-axial plane, and (b) structure of a single-chain (1-D) PE crystal.

selecting an appropriate mesh size and the corresponding smearing factor can be problematic, and until now there was no well-recognized rigorous way to select the appropriate combination, although this is much less challenging for the 3-D systems. More importantly, the results of the single PE chain using Gaussian smearing were found to be quite sensitive to the choice of the smearing factor even at a large mesh size. So, we developed the hyperspace tetrahedron method based on the linear tetrahedron method[39,47,48] for the Dirac delta function (details can be found in the ESI†), the accuracy of which only depends on the mesh size, therefore avoiding an arbitrary smearing factor. This method estimates the double integral $\iint Q_{\mathbf{q},\mathbf{q}'}\delta(\omega_{\mathbf{q}}-\omega_{\mathbf{q}'})\mathrm{d}\mathbf{q}\mathrm{d}\mathbf{q}'$, where Q can be any parameter related to $\mathbf{q}$ and $\mathbf{q}'$, in a hyperspace $\mathbf{q}\otimes\mathbf{q}'$, which is discretized subsequently in this higher dimensional space $\left(\iint Q_{\mathbf{q},\mathbf{q}'}\delta(\omega_{\mathbf{q}}-\omega_{\mathbf{q}'})\mathrm{d}\mathbf{q}\mathrm{d}\mathbf{q}' \rightarrow \int_{\mathbf{q}\otimes\mathbf{q}'} Q_{\mathbf{q},\mathbf{q}'}\delta(\omega_{\mathbf{q}}-\omega_{\mathbf{q}'})\mathrm{d}S_{\mathbf{q},\mathbf{q}'}\right)$. This method gives a finite scattering rate of collinear scattering events while the conventional linear tetrahedron method yields an infinite estimation of collinear scatterings which satisfy the energy conservation intrinsically. Moreover, this method can avoid the asymmetric problem $\delta(\omega_{\mathbf{q}}-\omega_{\mathbf{q}'}) \neq \delta(\omega_{\mathbf{q}'}-\omega_{\mathbf{q}})$ in the linear tetrahedron method, thus keeping the interchangeability of the three phonons in the scattering probability $P^{\lambda''}_{\lambda,\lambda'}$. Violations might lead to the breakdown of the positive-definite property of the collision matrix[34] and result in a false divergent thermal conductivity calculation.

Results and discussion

The fully relaxed PE crystal has an orthorhombic structure as shown in Fig. 1(a). The parameters a, b and c are lattice constants and θ is the chain setting angle (the dihedral angle between the plane of carbon atoms on a single chain and the xz plane). The predicted lattice parameters (a = 6.98 Å, b = 4.85 Å, c = 2.55 Å, θ = 43.3°) have been compared with experiments (see the ESI, Table S1†) with the maximum deviation of less than 2%, verifying the accuracy of the first-principles calculations in predicting the bulk PE crystal structure. As for an individual PE chain [Fig. 1(b)], the lattice parameter c varies a little (2.53 Å) compared with that in bulk PE (2.55 Å).

Dispersion relations

Starting from the equilibrium positions, the phonon dispersion and density of states (DOS, D_p) of both bulk and single-chain PE were calculated and are shown in Fig. 2(a) and (b).

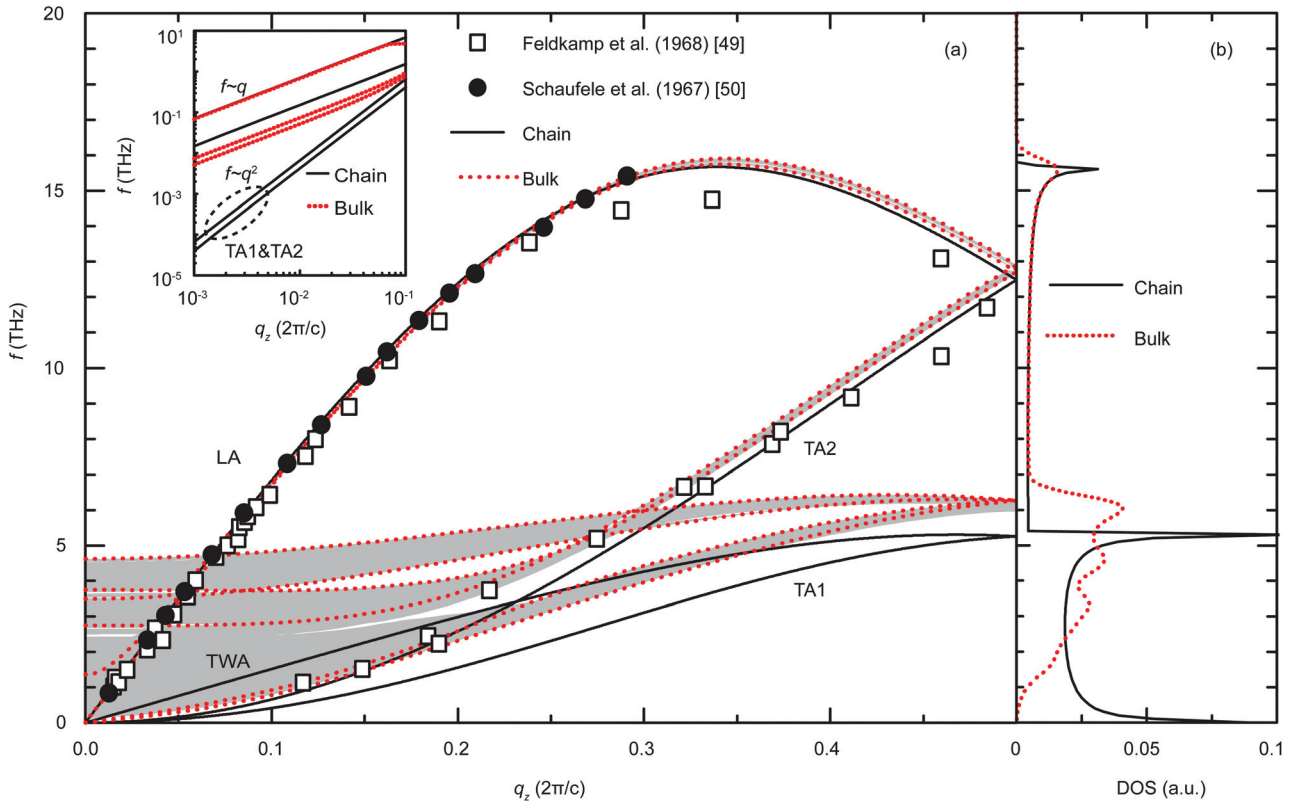

Fig. 2 (a) Phonon dispersion of a 1-D PE chain (along the chain) at low frequencies. TA1 and TA2 are the two transverse phonon modes vibrating perpendicular to the chain axis, TWA is the twisting mode and LA is the longitudinal mode. The phonon dispersion of the bulk PE crystal from Γ to Z is shown as dotted curves while all dispersion curves of the bulk PE from q_z = 0 to q_z = π/c are projected as the shaded area. Experimental dispersion curves[49,50] of bulk PE are also displayed in comparison. The inset compares the dispersion in the vicinity of Γ on a logarithmic scale. (b) Phonon DOS of a 1-D chain and bulk PE. (DOS is normalized to make the total number of states equal to one.)

Although the highest frequency reaches 90 THz (the full dispersion is shown in ESI Fig. S2†), most phonons of frequency >20 THz are caused by the strong localized interactions of C–C and C–H bonds, which lead to small group velocities and negligible contributions to the lattice thermal conductivity. Therefore, only low-frequency dispersion branches (below 20 THz) are shown in Fig. 2. There are 4 acoustic phonon modes of 1-D PE shown in Fig. 2(a), namely one longitudinal acoustic (LA), one twisting acoustic (TWA) and two transverse acoustic (TA) modes. In bulk PE, the corresponding number of modes is 8 as a result of the split acoustic phonons due to inter-chain interactions in bulk PE.

For the bulk PE crystal, the good coincidence of predicted dispersion relations with experiments in Fig. 2(a) validates the calculated harmonic force constants. The group velocity of LA phonons along the chain is rather high (17 km s^{-1}, close to that of diamond and carbon nanotubes), due to the strong axial C–C covalent bonds, which also account for the large axial Young's modulus (330.7 GPa in this study). Such a high group velocity is expected to boost phonon transport in crystalline PE and is also the main reason why a larger crystallinity often results in a higher axial thermal conductivity.[4,9] However, optical phonons with frequency below 5 THz have rather small group velocities and are intertwined with each other, which is more prominent when all the dispersion curves from $(x, y, 0)$ to $(x, y, \pi/c)$ (x and y are arbitrary) in the Brillouin zone of bulk PE are projected and shown as a shaded area in Fig. 2(a). Contrary to frequency gaps in dispersion relations which lower the chance of phonon–phonon coupling,[51] the phonon dispersion intertwinement makes it more probable for energy and momentum conservations to be satisfied and thus enlarges the space of the three-phonon scatterings. On the other hand, as the bulk PE crystal reduces to a single chain, the lack of split optical modes in 1-D PE makes the effective group velocity larger at the corresponding frequencies (2–5 THz) and the scattering phase space smaller.

The difference in dispersion is more influential on the transverse modes with long wavelengths, as shown in the inset of Fig. 2(a). The two TA modes of the 1-D PE chain have quadratic dispersions, while those of the LA and TWA modes are linear. By comparison, the dispersions of bulk PE are linear for all the acoustic phonons at small wavevectors. For a fully relaxed 1-D structure without any internal stress, the 1-D chain can be considered as an infinitely long rod in the long-wavelength limit and acoustic vibrations degrade to the classic continuum model for rods with quadratic transverse dispersions.[52] Therefore, the dispersion relations of the two TA modes are expected to be quadratic in a 1-D chain structure, the same as the ZA mode in 2-D structures such as graphene and borophene.[45] This difference impacts the DOS (D_p) at low frequencies. From the definition of D_p in ref. 36, the bulk PE with a linear dispersion relation follows the relation $D_p \sim \omega^2$, while for the 1-D chain with a quadratic dispersion the relation is $D_p \sim \omega^{-1/2}$. As illustrated in Fig. 2(b), the D_p of bulk PE approaches 0 for frequencies lower than 1 THz, while in 1-D PE it tends to diverge with the decrease of frequency.

Thermal conductivity of the bulk PE crystal

With the calculated harmonic properties, anharmonic lattice dynamics calculations were conducted with a careful validation process of the thermal expansion coefficients (see ESI Fig. S3†). Thermal conductivity of bulk PE was acquired thereafter. Fig. 3(a) shows the predicted axial κ of the bulk PE crystal as a function of temperature in all the directions (convergence tests with respect to the mesh size are shown in ESI Fig. S4†). The results from the exact solution of the BTE are only around 20% higher than the predictions from the SMRT model for $T > 200$ K, but for $T < 200$ K the difference becomes

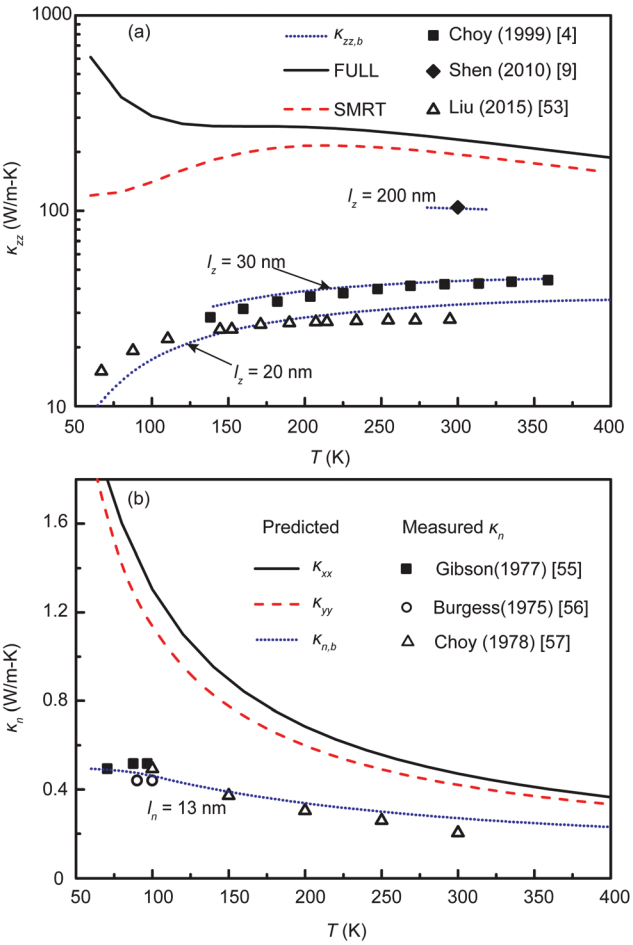

Fig. 3 (a) Variation of the axial thermal conductivity of the PE bulk crystal with respect to temperature. Results from the full BTE and the single-mode relaxation-time (SMRT) model are shown. The axial thermal conductivities accounting for boundary scatterings ($\kappa_{zz,b}$) with different lamina lengths (l_z) are compared with previous measurements.[4,9,53] l_z = 20 nm is given in the compared experimental study,[53] while l_z = 30 nm and l_z = 200 nm are fitted from the corresponding experimental studies in comparison, respectively. (b) The same as (a) for the cross-axial thermal conductivity (κ_{xx}, κ_{yy} and κ_n), where κ_n is the normal thermal conductivity to the chain axis. The predicted normal thermal conductivity of nanocrystallites ($\kappa_{n,b}$) adopts the crystallite thickness (l_n) value of 13 nm also given by ref. 53 The results from the SMRT vary little from the full BTE solution for the cross-axial thermal conductivity and are thus not shown. The dotted points are κ_n values extracted from the experimental studies.[55–57]

much larger. This is because high-frequency phonon modes, including those at the edge of the Brillouin zone, are not excited for $T < 200$ K, which significantly reduces the Umklapp scatterings and leads to a large underestimation of κ using the SMRT model.

The predicted axial κ_{zz} is 237 W m^{-1} K^{-1} at room temperature, in between the classical MD prediction values of 47 to 310 W m^{-1} K^{-1},[12,13] but significantly higher than all the reported experimental values (*e.g.* 104 W m^{-1} K^{-1},[9] 41 W m^{-1} K^{-1} (ref. 4) and 27 W m^{-1} K^{-1} (ref. 53)). This can be due to the non-ideal crystals in the experiments. The isotope effects on κ are modest for bulk PE (around 10% κ reduction at 300 K). The axial crystallite lengths (l_z) for the semi-crystalline PE are often rather small (8–42 nm (ref. 54)). Therefore, the crystallite boundaries suppress the phonon transport and lead to a much lower thermal conductivity. Once the phonon boundary scatterings from the crystallite boundaries is included using the same crystallite length (20 nm) measured in ref. 53, through eqn (5) the calculated $\kappa_{zz,b}$ (axial thermal conductivity with boundary scattering) matches well with the measurements in the same study. Since the size of axial crystallites depends on the draw ratio and the preparation method and may reach as high as 3 μm,[4] experimentally recorded κ_{zz} results span rather widely as shown in Fig. 3(a). By using the crystallite size fitted from the measured κ_{zz} value at 300 K, the calculation results agree well with the experimental results[4,9,53] from different groups over a wide temperature range. The coincidence between other predicted $\kappa_{zz,b}$ and the fitted crystallite lengths and measurements on different PE samples reveals different estimated sample qualities and the potential for further improvement.

It is also observed that κ is strongly anisotropic. In Fig. 3(b), the cross-axial value is almost three orders lower than the axial value near room temperature. The small κ_{xx} and κ_{yy} are due to the weak vdW interactions across chains, which result in low group velocities and strong anharmonic scatterings. The average of the predicted cross-axial κ_{xx} and κ_{yy} (*i.e.*, the normal thermal conductivity κ_n) is about 0.45 W m^{-1} K^{-1} at room temperature, two times that from the experiments (~0.22 W m^{-1} K^{-1} (ref. 23 and 58)). This discrepancy becomes more pronounced at lower temperatures, which is also attributed to the small sizes of the nanocrystallites (~13 nm (ref. 53)) in the semi-crystalline PE samples used in the experiments. Similar to the axial κ, the inclusion of the boundary effect with the above thickness retrieves the trend of measured data at different temperatures, as shown in Fig. 3(b). Note that the model with boundary scatterings for real PE samples only serves as a rough approximation at low temperatures. In the synthesized PE samples, microcrystals are less oriented and connected by amorphous taut-tie chains. These taut-tie chains vibrate with large amplitude at high temperatures and arouse much larger scatterings. The behavior of phonons in real PE crystals at elevated temperatures awaits further investigation.

The thermal conductivity of 1-D PE was obtained and is shown in Fig. 4(a) and (b). The solution of BTE takes many more iteration steps than those for bulk PE, indicating much more harmonic nature of the 1-D PE chain (ESI Fig. S7†). It is seen in Fig. 4(a) that the SMRT model significantly underestimates the thermal conductivity of the single-chain PE over the entire considered temperature range. Such an underestimation is a result of dominant normal (momentum-conserving) phonon scattering processes in the single-chain PE as in the bulk PE at low temperatures or some 2-D materials,[59] since the SMRT simply treats both the normal and Umklapp processes as dissipation sources.

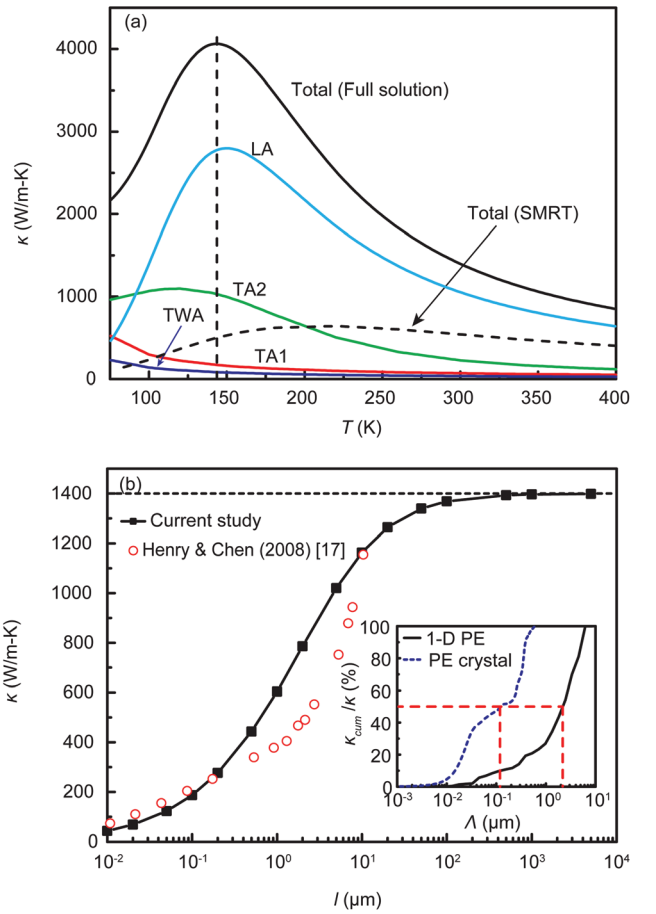

Fig. 4 (a) Variations of the axial thermal conductivity of an infinite 1-D PE chain as a function of temperature, along with the absolute κ contributions from the four acoustic phonon modes and the κ values from the SMRT model; κ contributions from optical phonons are negligible and are thus not shown. (b) Variation of the axial thermal conductivity of the 1-D PE chain at 300 K as a function of chain length l. Inset of (b): normalized cumulative axial thermal conductivity with the distribution of the phonon mean free path Λ.

The large κ of an infinite chain at different temperatures are predicted to be convergent, and the value at room temperature is 1400 W m^{-1} K^{-1}. This value appears modest compared with the κ values of other carbon-based materials, *e.g.*, graphene and carbon nanotubes,[5] but it is close to that of graphene (fully hydrogenated graphene). It is probably due to the buckled PE chain structure and the H atoms bonded to C. A reduction in κ due to the hydrogenation in graphene, which induces buckling of the carbon backbone, has been observed,

and suppressed effective group velocities and additional scatterings of low-frequency phonons explain this effect.[60,61]

The absolute value of κ is almost 4 orders of magnitude higher than that of amorphous PE and 6 times that of the bulk PE. This enhancement is mainly caused by the reduction of scattering phase space due to the disappearance of inter-chain vdW forces. The modal contributions from each phonon branch are also shown in Fig. 4(a) and reveal a much smaller κ contribution from the TA1 and TA2 modes with quadratic dispersions compared with the LA mode. This is in sharp contrast with the dominant role of the quadratic flexural mode (ZA) in the heat transfer in graphene (contributing as high as 88%[25]). Such minor contributions from the quadratic branches are attributed to the small group velocity at low frequencies, and more importantly, to the limited phonon lifetimes influenced by strong normal scatterings, which would be revisited later.

The $\kappa(T)$ peaks at around 145 K, which is due to the counterbalance between the heat capacity and the anharmonic scattering, especially for the LA and TA2 phonon modes. At high temperatures, all the phonons are excited and the heat capacity is saturated and κ decreases with the increase of temperature (stronger anharmonic scatterings), while at lower temperatures the heat capacity decreases (reduction of excited phonons impairs thermal transport).

The convergence of κ with respect to the chain length l is shown in Fig. 4(b) and κ reaches a plateau at around 1 mm. When l < 10 μm, the predictions match quite well with previous classical MD simulations.[17] The slow convergence of the κ of 1-D PE with the increase of chain length is explained by the large phonon mean free paths, as elucidated in the inset of Fig. 4(b). The half-contributing mean free path ($\Lambda_{1/2}$) extends from 0.12 μm in the bulk PE crystal to 2.2 μm in the 1-D PE. The results indicate that the κ of 1-D PE is even more sensitive to the sample size than the bulk PE.

To shed light on the high κ of the PE chain, the cumulative κ value with respect to the frequency is plotted in Fig. 5(a). It is found that κ is almost saturated at ~16 THz, indicating that the acoustic phonons dominate the thermal transport in the single-chain PE. Phonons with frequency lower than 5.5 THz (the cutoff frequency of TA1 and quadratic part of TA2) contribute only 14% to κ, much smaller compared with the contribution of the quadratic flexural mode (ZA) in graphene (as high as 88%[25]). The contrast is mainly due to the limited lifetimes of TA phonons of single-chain PE at low frequencies. The effective spectral lifetimes [defined in eqn (6)] in Fig. 5(b) show $\tau_{\text{eff}} \sim \omega^{-1}$ for both TA modes while a much more influential τ_{eff} (ZA) $\sim \omega^{-1.4}$ in graphene was extracted from ref. 25.

Such limited spectral lifetimes guarantee a finite κ contribution. Using the kinetic theory $\kappa = \int D_p(\omega)C_v(\omega)v^2(\omega)\tau_{\text{eff}}(\omega)\mathrm{d}\omega$, although D_{p} diverges as $\omega^{-1/2}$, $v \sim \omega^{1/2}$ at small wavevectors, as shown in Fig. 5(c), and the modal heat capacity C_v reaches the Boltzmann constant k_{B}. Given the relation τ_{eff} (TA) $\sim \omega^{-1}$, the κ contribution from low-frequency TA modes is $\kappa_{\text{TA}} \propto \int \omega^{-0.5}\mathrm{d}\omega$, which is finite with the integration starting from 0. Similarly, τ_{eff} of long-wavelength LA and TWA modes tends to be a constant and thus κ contributions from these modes are expressed as

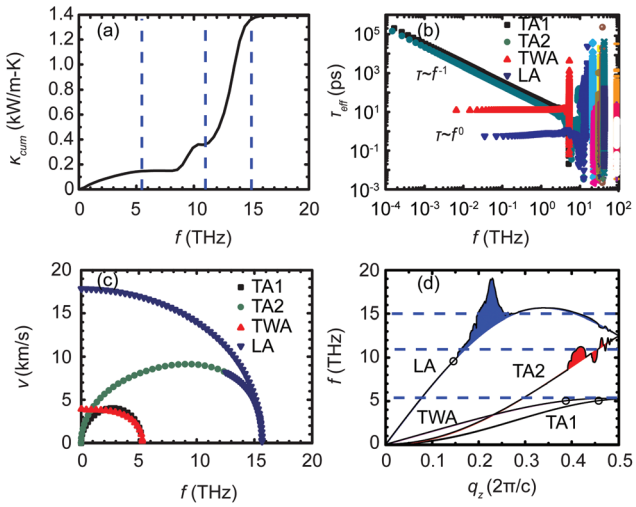

Fig. 5 (a) Cumulative axial thermal conductivity of the PE chain with respect to frequency. (b) Variations of modal effective lifetimes with respect to frequency (logarithmic scales). (c) Variation of the modal group velocity (absolute value) with frequency over 0 to 20 THz. (d) Dispersions with normalized modal contributions to the thermal conductivity shown as the vertical broadening of each phonon branch; the three small circles represent the three phonons participating in one possible Umklapp scattering event. The three horizontal dashed lines located at 5.5, 11 and 15 THz are used to differentiate phonons and their κ contributions. All theproperties are for 300 K.

$\kappa_{\text{LA(TWA)}} \propto \int \omega^0 \mathrm{d}\omega$. Therefore, both linear and quadratic phonon modes contribute finitely to κ and lead to a convergent thermal conductivity in an infinite PE chain. The convergence behaviors of TAs and TWA modes are consistent with the previous studies on the "rotator model",[14] in which the potential energy is proportional to the chain distortion angles. As for the LA mode, the 1-D Fermi–Pasta–Ulam (FPU) model[15] is often adopted in the literature to simulate the heat transport, and divergence is sometimes observed. However, contrary to the 1-D FPU model with either 1-D vibrations[62] or nearest-neighbor interactions,[16] the single-chain lattice vibrates in the 3-D space and thus the transverse and twisting motions arise. The additional inter-mode scatterings significantly increase the scattering phase space and serve as dissipative sources for the vibrational energy transport.

Moreover, from the relative κ contribution $\bar{\kappa}_\lambda \left(\sum_\lambda \bar{\kappa}_\lambda = 1\right)$ from phonons on each dispersion band in Fig. 5(d), one can easily find that the room-temperature thermal conductivity is mainly contributed by the LA phonons with frequency ranging from 11 to 15 THz, as also found in Fig. 4(a) from its dominant contribution. Over this range below the LA cutoff frequency, the LA group velocity maintains relatively large. However, LA modes with lower frequencies (5.5 to 11 THz) and larger group velocities only account for a small portion of the thermal conductivity. This phenomenon is a result of the strong Umklapp scattering involving the twisting and transverse modes, *e.g.*, LA → TWA + TA1, with the three involved phonons shown as three small circles on Fig. 5(d). This scattering channel is

blocked once the LA phonon frequency surpasses double the cutoff of TWA and TA1, making the LA phonons above 11 THz dominant in the κ contribution.

It is noted that this Umklapp scattering channel is reported to be impossible in carbon nanotubes due to the selection rule imposed by the conservation of angular momentum[28] However, due to the $C_{2h}{}^2$ symmetry nature of the quasi-1-D PE chain, there are only two cyclic angular momentum indices, 0 and 1 (±1 are equivalent).[63] It is easy to check that any combination of three phonons satisfies the conservation law of angular momentum (clearly, a periodicity number 2 is sometimes needed).

The Umklapp scattering is considered to be not only the main reason for the low κ contribution from phonons lying within 5.5 to 11 THz, but also the source of convergent κ contribution from long-wavelength phonons. As for phonons below 5.5 THz, even though these long-wavelength phonons hardly experience the Umklapp scatterings, there exist other normal scatterings, for example, the intrinsically satisfied collinear scatterings LA → LA + LA, TWA → TWA + TWA and other noncollinear scatterings (*e.g.* TWA → TA1 + TA2, LA → TA1 + TA1 and LA → TA2 + TA2). The large normal scatterings contribute indirectly to energy dissipation by dragging phonons to the frequency range where the Umklapp scattering is more probable. Therefore, it leads to finite effective relaxation times at low frequencies as shown in Fig. 5(b), and eventually a finite thermal conductivity contribution.

To understand the phonon scattering channels and the roles of the normal (N) and Umklapp (U) processes in phonon transport, the scattering matrix $\tilde{\mathbf{P}}$ of 3-phonon processes as defined in eqn (4) is plotted in Fig. 6. The wavevector q ranges from $-G/2$ to $G/2$ ($G = 2\pi/c$ for single-chain PE) for each phonon branch. Therefore, for any point (q, q') found on the contour map, the third phonon q'' that participates in the scattering can be uniquely determined by the momentum conservation law (q'' also lies in the range from $-G/2$ to $G/2$). It is found that this matrix is not diagonally dominant, which explains the failure of the SMRT approximation that only considers the diagonal scatterings.[36] The scatterings among TA1, TA2 and TWA are discernably much stronger than those of LA phonons. In particular, the TWA branch acts as the scattering center among the acoustic phonons, generating a large phase space in the lowest 3 acoustic phonon branches. Therefore, the thermal conductivity contributions from the TA and TWA branches are much smaller than that from the LA branch.

Moreover, the finite thermal conductivity in single-chain PE can also be explained by analyzing the N and U scatterings which can be distinguished in Fig. 6. For example, the (TA1, TA1) region is divided into three zones by the dashed line $|q + q'| = G/2$. Scattering events lying within the two dashed lines are N and the two triangular areas are dissipative U processes. This also applies to other regions. Although the major scatterings of phonons near the Γ point are N processes, the U processes are not rare for the acoustic phonons in the single-chain PE, especially for the TA1, TA2 and TWA phonons. This explains the finite thermal conductivity contributions

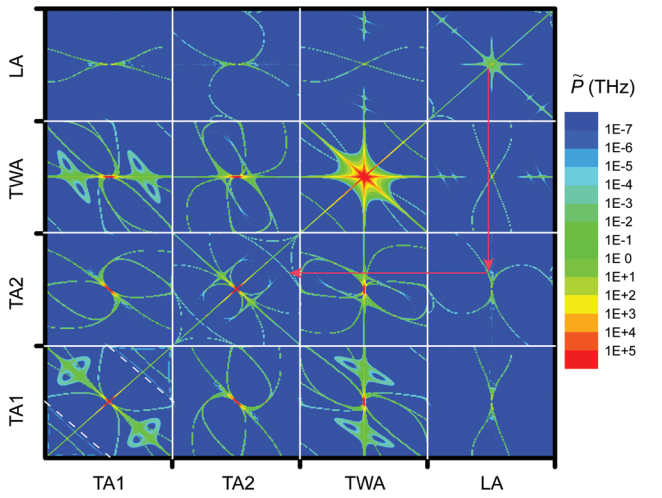

Fig. 6 Contour plot of the scattering matrix ($\tilde{\mathbf{P}}$) among acoustic phonons. The scatterings between acoustic and optical phonons are found to be rather small and are thus not shown. Each phonon branch index contains all **q**-points with q_z from $-G/2$ to $G/2$ ($G = 2\pi/c$). Each point is specified as a pair (q, q'). Only the scatterings among the acoustic phonons are plotted. The white dashed line in (TA1, TA1) denotes the boundaries between normal ($|q + q'| < G/2$) and Umklapp ($|q + q'| > G/2$) scatterings. The red arrow exemplifies one consecutive scattering channel for low-wavevector LA phonons to indirectly experience Umklapp scatterings.

from these three branches. As for the LA phonons with small wavevectors, it is seen that the off-diagonal normal couplings in the LA phonons remain quite strong, which can indirectly contribute to the U processes if it follows consecutive scattering events exemplified with the red arrows. Therefore, the thermal conductivity contributions from all acoustic phonons should behave normal and remain finite due to the finite Umklapp scatterings and the indirect contribution from the strong normal processes.

Conclusions

We calculated the thermal conductivity of the bulk PE crystal and the 1-D PE chain by solving the Boltzmann transport equation with the interatomic force constants from the first principles calculations. The calculated axial thermal conductivity of the bulk PE crystal is 237 W m^{-1} K^{-1} at room temperature. Free from the strong anharmonic inter-chain van der Waals forces, a single PE chain has a much higher thermal conductivity (1400 W m^{-1} K^{-1} at 300 K). The thermal conductivity of the PE chain is convergent, due to the indirect thermal resistance from the normal 3-phonon scatterings and the cross-couplings between different phonon branches. The dominant thermal conductivity contribution is from the high-frequency LA phonons, due to the relatively large group velocity and the low scattering rate with the low-frequency phonons. The phonon transport analysis sheds light on the molecular-level design of polymers for enhanced thermal performance.

Conflicts of interest

There are no conflicts to declare.

Acknowledgements

We are thankful for the financial support from the Hong Kong General Research Fund (Grant No. 613413 and 16213015) and Science and Technology Planning Project of Guangdong Province, China (Grant No. 2016A050503001). X. W. is thankful for the discussions with Jesús Carrete Montaña about the symmetry constraints and their influence on the phonon dispersion relation in 1-D and 2-D materials. M. K. is grateful to the US National Science Foundation for support (Thermal Transport and Processes Program Award No. CBET1332807).

References

1 X. Huang, P. Jiang and T. Tanaka, *IEEE Electr. Insul. Mag.*, 2011, **27**, 8–16.
2 B. Lee, *eXPRESS Polym. Lett.*, 2008, **2**, 357–363.
3 H. Chen, V. V. Ginzburg, J. Yang, Y. Yang, W. Liu, Y. Huang, L. Du and B. Chen, *Prog. Polym. Sci.*, 2016, **59**, 41–85.
4 C. L. Choy, Y. W. Wong, G. W. Yang and T. Kanamoto, *J. Polym. Sci., Part B: Polym. Phys.*, 1999, **37**, 3359–3367.
5 A. A. Balandin, *Nat. Mater.*, 2011, **10**, 569–581.
6 L. Lindsay and D. A. Broido, *Phys. Rev. B: Condens. Matter*, 2012, **85**, 035436.
7 L. Lindsay, D. A. Broido and N. Mingo, *Phys. Rev. B: Condens. Matter*, 2011, **83**, 235428.
8 D. Singh, J. Y. Murthy and T. S. Fisher, *J. Appl. Phys.*, 2011, **110**, 044317.
9 S. Shen, A. Henry, J. Tong, R. Zheng and G. Chen, *Nat. Nanotechnol.*, 2010, **5**, 251–255.
10 K. Liu, Y. Song, W. Feng, N. Liu, W. Zhang and X. Zhang, *J. Am. Chem. Soc.*, 2011, **133**, 3226–3229.
11 T. Meier, F. Menges, P. Nirmalraj, H. Hölscher, H. Riel and B. Gotsmann, *Phys. Rev. Lett.*, 2014, **113**, 060801.
12 A. Henry, G. Chen, S. J. Plimpton and A. Thompson, *Phys. Rev. B: Condens. Matter*, 2010, **82**, 144308.
13 B. Ni, T. Watanabe and S. R. Phillpot, *J. Phys.: Condens. Matter*, 2009, **21**, 084219.
14 M. J. Gillan and R. W. Holloway, *J. Phys. C: Solid State Phys.*, 1985, **18**, 5705.
15 E. Fermi, J. Pasta and S. Ulam, *Los Alamos Rep.*, 1940, 124–139.
16 J.-S. Wang and B. Li, *Phys. Rev. Lett.*, 2004, **92**, 074302.
17 A. Henry and G. Chen, *Phys. Rev. Lett.*, 2008, **101**, 235502.
18 T. Luo, K. Esfarjani, J. Shiomi, A. Henry and G. Chen, *J. Appl. Phys.*, 2011, **109**, 074321.
19 H. Guo-Jie, C. Bing-Yang and L. Yuan-Wei, *Chin. Phys. Lett.*, 2014, **31**, 086501.
20 J. Liu and R. Yang, *Phys. Rev. B: Condens. Matter*, 2012, **86**, 104307.
21 A. Henry and G. Chen, *Phys. Rev. B: Condens. Matter*, 2009, **79**, 144305.
22 J.-W. Jiang, J. Zhao, K. Zhou and T. Rabczuk, *J. Appl. Phys.*, 2012, **111**, 124304.
23 D. B. Mergenthaler, M. Pietralla, S. Roy and H. G. Kilian, *Macromolecules*, 1992, **25**, 3500–3502.
24 D. P. Sellan, E. S. Landry, J. E. Turney, A. J. H. McGaughey and C. H. Amon, *Phys. Rev. B: Condens. Matter*, 2010, **81**, 214305.
25 Y. Kuang, L. Lindsay, S. Shi, X. Wang and B. Huang, *Int. J. Heat Mass Transfer*, 2016, **101**, 772–778.
26 M. C. Payne, M. P. Teter, D. C. Allan, T. A. Arias and J. D. Joannopoulos, *Rev. Mod. Phys.*, 1992, **64**, 1045–1097.
27 R. Guo, X. Wang, Y. Kuang and B. Huang, *Phys. Rev. B: Condens. Matter*, 2015, **92**, 115202.
28 L. Lindsay, D. A. Broido and N. Mingo, *Phys. Rev. B: Condens. Matter*, 2009, **80**, 125407.
29 X. Wang, R. Guo, D. Xu, J. D. Chung, M. Kaviany and B. Huang, *J. Phys. Chem. C*, 2015, **119**, 26000–26008.
30 H. Xie, M. Hu and H. Bao, *Appl. Phys. Lett.*, 2014, **104**, 131906.
31 N. Mingo and D. A. Broido, *Nano Lett.*, 2005, **5**, 1221–1225.
32 W. Li, J. Carrete, N. A. Katcho and N. Mingo, *Comput. Phys. Commun.*, 2014, **185**, 1747–1758.
33 D. A. Broido, M. Malorny, G. Birner, N. Mingo and D. A. Stewart, *Appl. Phys. Lett.*, 2007, **91**, 231922.
34 L. Chaput, *Phys. Rev. Lett.*, 2013, **110**, 265506.
35 K. Hippalgaonkar, B. Huang, R. Chen, K. Sawyer, P. Ercius and A. Majumdar, *Nano Lett.*, 2010, **10**, 4341–4348.
36 G. P. Srivastava, *The Physics of Phonons*, CRC Press, 1990.
37 N. Bonini, J. Garg and N. Marzari, *Nano Lett.*, 2012, **12**, 2673–2678.
38 G. Fugallo, M. Lazzeri, L. Paulatto and F. Mauri, *Phys. Rev. B: Condens. Matter*, 2013, **88**, 045430.
39 A. Togo, L. Chaput and I. Tanaka, *Phys. Rev. B: Condens. Matter*, 2015, **91**, 094306.
40 J. Klimeš, D. R. Bowler and A. Michaelides, *J. Phys.: Condens. Matter*, 2010, **22**, 022201.
41 J. Klimeš, D. R. Bowler and A. Michaelides, *Phys. Rev. B: Condens. Matter*, 2011, **83**, 195131.
42 G. Kresse and J. Furthmüller, *Phys. Rev. B: Condens. Matter*, 1996, **54**, 11169–11186.
43 G. Kresse and J. Furthmüller, *Comput. Mater. Sci.*, 1996, **6**, 15–50.
44 K. Esfarjani and H. T. Stokes, *Phys. Rev. B: Condens. Matter*, 2008, **77**, 144112.
45 J. Carrete, W. Li, L. Lindsay, D. A. Broido, L. J. Gallego and N. Mingo, *Mater. Res. Lett.*, 2016, 1–8.
46 N. Mingo, D. Stewart, D. Broido and D. Srivastava, *Phys. Rev. B: Condens. Matter*, 2008, **77**, 033418.
47 A. H. MacDonald, S. H. Vosko and P. T. Coleridge, *J. Phys. C: Solid State Phys.*, 1979, **12**, 2991.
48 A. Togo, F. Oba and I. Tanaka, *Phys. Rev. B: Condens. Matter*, 2008, **78**, 134106.
49 L. A. Feldkamp, G. Venkataraman and J. S. King, in *Neutron Inelastic Scattering Vol. II. Proceedings of a Symposium on*

Neutron Inelastic Scattering, International Atomic Energy Agency, Vienna (Austria), Copenhagen, Denmark, 1968, vol. 44, pp. 159–165.
50 R. F. Schaufele and T. Shimanouchi, *J. Chem. Phys.*, 1967, **47**, 3605–3610.
51 S. Lee, K. Esfarjani, T. Luo, J. Zhou, Z. Tian and G. Chen, *Nat. Commun.*, 2014, **5**, 3525.
52 E. M. Lifshitz, A. M. Kosevich and L. P. Pitaevskii, *in Theory of Elasticity*, Butterworth-Heinemann, Oxford, *3rd edn*, 1986, pp. 87–107.
53 J. Liu, Z. Xu, Z. Cheng, S. Xu and X. Wang, *ACS Appl. Mater. Interfaces*, 2015, **7**, 27279–27288.
54 G. T. Davis, R. K. Eby and J. P. Colson, *J. Appl. Phys.*, 1970, **41**, 4316–4326.
55 A. G. Gibson, D. Greig, M. Sahota, I. M. Ward and C. L. Choy, *J. Polym. Sci., Polym. Lett. Ed.*, 1977, **15**, 183–192.
56 S. Burgess and D. Greig, *J. Phys. C: Solid State Phys.*, 1975, **8**, 1637.
57 C. L. Choy, W. H. Luk and F. C. Chen, *Polymer*, 1978, **19**, 155–162.
58 C. L. Choy, F. C. Chen and W. H. Luk, *J. Polym. Sci., Polym. Phys. Ed.*, 1980, **18**, 1187–1207.
59 S. Lee, D. Broido, K. Esfarjani and G. Chen, *Nat. Commun.*, 2015, **6**, 6290.
60 A. Cepellotti, G. Fugallo, L. Paulatto, M. Lazzeri, F. Mauri and N. Marzari, *Nat. Commun.*, 2015, **6**, 6400.
61 L. Lindsay and Y. Kuang, *Phys. Rev. B: Condens. Matter*, 2017, **95**, 121404.
62 S. Chen, J. Wang, G. Casati and G. Benenti, *Phys. Rev. E: Stat. Phys., Plasmas, Fluids, Relat. Interdiscip. Top.*, 2014, **90**, 032134.
63 V. N. Popov, V. E. Van Doren and M. Balkanski, *Phys. Rev. B: Condens. Matter*, 2000, **61**, 3078.